

Tri-spectral decoupled programmable thermal emitter for multimode camouflage with heterogeneous phase-change integration

Sihong Zhou ^{a, b, c}, Shikui Dong ^{a, b}, Jiameng Song ^{a, b}, Yanming Guo ^{a, b}, Yong Shuai ^{a, b, *} and Guangwei Hu ^{c, d, *}

^a*Key Laboratory of Aerospace Thermophysics of Ministry of Industry and Information Technology, Harbin 150001, China*

^b*School of Energy Science and Engineering, Harbin Institute of Technology, Harbin 150001, China*

^c*School of Electrical and Electronic Engineering, 50 Nanyang Avenue, Nanyang Technological University, Singapore, 639798, Singapore*

^d*CNRS-International-NTU-Thales Research Alliance (CINTRA), IRL 3288, 50 Nanyang Drive, Singapore 637553, Singapore*

E-mail address: guangwei.hu@ntu.edu.sg, shuaiyong@hit.edu.cn

S1. The coordinates calculation method of visible color in CIE 1931

The detailed coordinates (x , y) calculation is as follows:

$$x = \frac{X}{X + Y + Z} \quad (\text{S1a})$$

$$y = \frac{Y}{X + Y + Z} \quad (\text{S1b})$$

Where X , Y , and Z are three stimulus values for three primary colors (red, green, and blue) and can be expressed as :

$$X = 100 \frac{\int_{\lambda} S(\lambda) R(\lambda) \bar{x}(\lambda) d\lambda}{\int_{\lambda} S(\lambda) \bar{y}(\lambda) d\lambda} \quad (\text{S2a})$$

$$Y = 100 \frac{\int_{\lambda} S(\lambda) R(\lambda) \bar{y}(\lambda) d\lambda}{\int_{\lambda} S(\lambda) \bar{y}(\lambda) d\lambda} \quad (\text{S2b})$$

$$Z = 100 \frac{\int_{\lambda} S(\lambda) R(\lambda) \bar{z}(\lambda) d\lambda}{\int_{\lambda} S(\lambda) \bar{y}(\lambda) d\lambda} \quad (\text{S2c})$$

Where $S(\lambda)$ is the standard energy intensity distribution of the D65 light source, and \bar{x} , \bar{y} , \bar{z} are the CIE matching functions, which are all shown in Fig. 1a.

S2. The MODTRAN setting parameters, the direct solar radiation and self-radiation intensity, and the atmosphere transmittance.

In this work, we use the US Standard 1976 atmosphere model in MODTRAN to calculate the solar radiation, and the detailed parameters are shown in Table S1:

Table. S1 MODTRAN's parameters in our letter

Parameters	
Water Column [cm]	1762.3
Ozone Column [cm]	0.34356
CO ₂ [ppmv]	400
CO [ppmv]	0.15
CH ₄ [ppmv]	1.8
Ground Temperature [K]	300
Ground Albedo	0
Aerosol Model	Desert
Visibility [km]	75.75

According to these parameters, we can calculate the direct solar spectral radiation $I_{\text{solar}}(\lambda)$ and the blackbody thermal radiation intensity at 22.5 °C and 175 °C in 3-5 μm and 8-14 μm shown as Fig. S1a.

When the object temperature is 22.5 °C, the self-radiation intensity is lower than the direct solar radiation in 3-5 μm . Therefore, for the radiation signal received by the detector, the solar radiation occupies the main position, and the device with a higher emissivity will reflect lower solar radiation, so the infrared image displayed by the detector will be shown as a lower signal intensity. On the contrary, when the object temperature is up to 175 °C, the self-radiation intensity is much higher than the direct solar radiation. So, the higher the emissivity of the object, the stronger the overall radiation signal.

Using MODTRAN, we also calculate the spectral atmospheric transmittance and the average atmospheric transmittance for two detection bands at different heights above the ground, as shown in Fig. S1b and S1c. It is evident that as height increases, atmospheric transmittance gradually decreases. At the atmospheric boundary 16,000 m above the ground, the average transmittance in the 3-5 μm band decreases from 0.91997 (at 10 m above the ground) to 0.55869, reducing 44.13%. In the 8-14 μm band, the average transmittance decreases from 0.99522 (at 10 m above the ground) to 0.74837, reducing 24.33%.

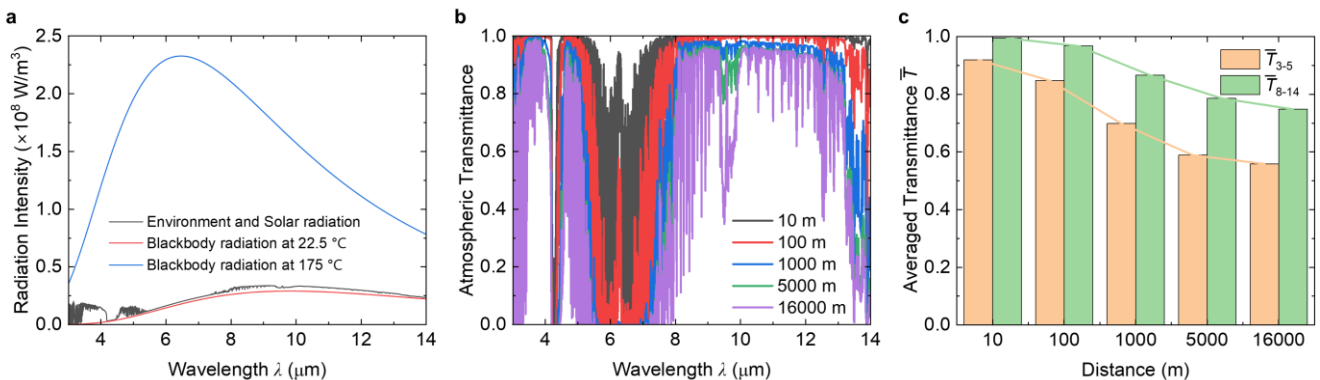


Fig. S1 **a.** The solar radiation intensity calculated by MODTRAN and the blackbody radiation intensity at 22.5 °C and 175 °C. **b.** The atmospheric transmittance at different heights above the ground. **c.** The averaged atmospheric transmittance in 3-5 and 8-14 μm at different heights above the ground.

S3. The IR spectral permittivity of IST and VO₂

The amorphous phase permittivity of IST (aIST) is considered as a Tauc-Lorentz model and the crystalline phase permittivity of IST (cIST) is considered as a Tauc-Lorentz-Drude model, which are both fitted from Heßler's experimental data at Nature Communications [1]. The detailed Tauc-Lorentz model with the imaginary part of the amorphous IST is described as:

$$\varepsilon_{\text{aIST_imag}} = \frac{A}{\omega} \frac{\omega_0 \gamma (\omega - \omega_g)^2}{(\omega^2 - \omega_0^2)^2 + \omega^2 \gamma^2} \Theta(\omega - \omega_g) \quad (\text{S3})$$

Where A is the resonator strength, ω is the angular frequency, ω_0 is the resonance frequency, γ is the resonator damping, ω_g is the band gap frequency, and the $\Theta(\omega - \omega_g)$ is the Heaviside function. The real part of the permittivity of aIST can be calculated by the Kramers-Kronig relations. While, for the crystalline phase permittivity of IST, a Drude term should be added to describe the metal-like properties of the crystalline phase IST:

$$\varepsilon_{\text{cIST_real}} = \text{real} \left(\frac{\omega_p^2}{\omega(\omega + i\gamma_D)} \right) + \varepsilon_{\text{aIST_real}} \quad (\text{S4a})$$

$$\varepsilon_{\text{cIST_imag}} = \text{imag} \left(\frac{\omega_p^2}{\omega(\omega + i\gamma_D)} \right) + \varepsilon_{\text{aIST_imag}} \quad (\text{S4b})$$

Where $\text{real}(\omega)$ means taking the real part of the results, $\text{imag}(\omega)$ means taking the imaginary part of the results, ω_p is the plasma frequency, and γ_D is the Drude damping.

The semiconducting-phase VO₂ (sVO₂) is an uniaxial anisotropic insulator, whose permittivity can be expressed as a tensor form with only principal diagonal elements:

$$\varepsilon_{\text{sVO}_2} = \begin{pmatrix} \varepsilon_O & 0 & 0 \\ 0 & \varepsilon_O & 0 \\ 0 & 0 & \varepsilon_E \end{pmatrix} \quad (\text{S5})$$

Where ε_O and ε_E are the permittivity for the incident electric field along and perpendicular to the optical axis direction[2]. For the spectral semiconducting-phase permittivity of VO₂, it can be calculated as the classical Lorentz oscillator expression from Ref. [3]:

$$\varepsilon(\omega) = \varepsilon_\infty + \sum_{j=1}^N \frac{S_j \omega_j^2}{\omega_j^2 - i\gamma_j \omega - \omega^2} \quad (\text{S6})$$

Where ε_∞ is the high-frequency constant, ω is the angular frequency, ω_j is the phonon vibration frequency, γ_j is the scattering rate, S_j represents the oscillation strength, and j is the mode index. And for the metallic-phase permittivity of VO₂, whose permittivity can be calculated as a classical Drude model:

$$\varepsilon_{\text{mVO}_2} = -\varepsilon_\infty \frac{\omega_p^2}{\omega^2 + i\omega\gamma} \quad (\text{S7})$$

In this work, we adopt the nine oscillators model for ε_E of sVO₂ and eight oscillators model for ε_O of sVO₂, and the detailed parameters for both sVO₂ and mVO₂ can be referred from Ref. [4]. The results of the permittivity of aIST and cIST are shown in Fig. S2a-b, and the results of the permittivity of sVO₂ and mVO₂ are shown in Fig. S2c-d.

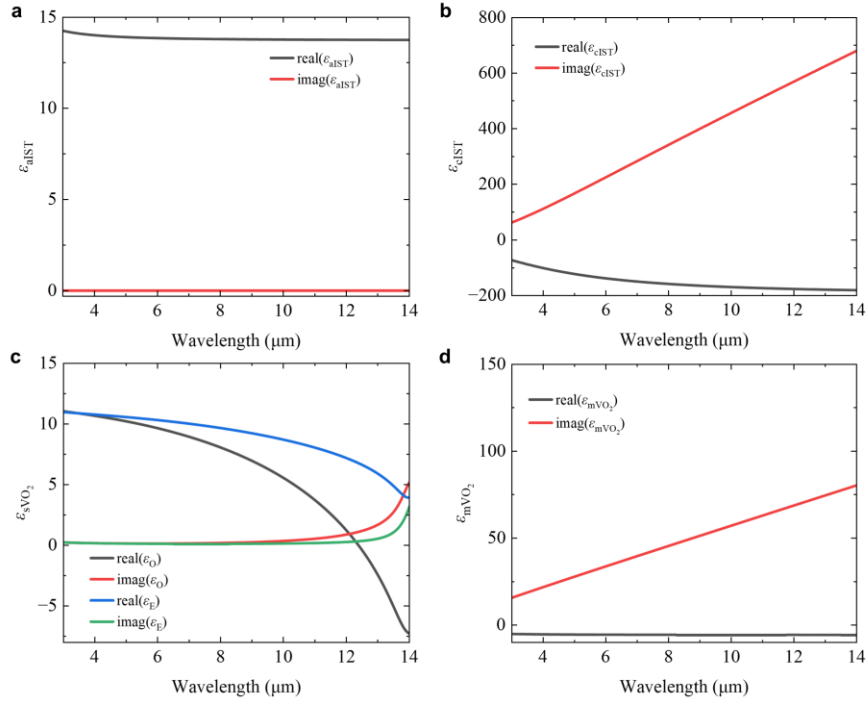


Fig. S2 The permittivity of (a). aIST, (b). cIST, (c). sVO₂ and (d). mVO₂

- [1] Heßler, A.; Wahl, S.; Leuteritz, T., et al. In₃SbTe₂ as a programmable nanophotonics material platform for the infrared. *Nature Communications* 2021, 12 (1), 1-10.
- [2] H. Wang, Y. Yang, L. Wang, et al. Switchable wavelength-selective and diffuse metamaterial absorber/emitter with a phase transition spacer layer. *Applied Physics Letters*, 2014, 105: 071907.
- [3] Y Yang, S. Basu, L. P. Wang. Radiation-based near-field thermal rectification with phase transition materials. *Applied Physics Letters*, 2013, 103: 163101.
- [4] A. S. Barker, Jr., H. W. Verleur, and H. J. Guggenheim. Infrared optical properties of vanadium dioxide above and below the transition temperature. *Physical Review Letters*, 1966, 17(26): 1286-1289.

S4. The metallization fraction and the effective permittivity of VO₂

The phase change process of VO₂ occurs gradually as the temperature increases and decreases, so the temperature-dependent metallization fraction f_{mVO_2} can be calculated as [1]:

$$f_{mVO_2} = \frac{1}{1 + \exp\left(\frac{W}{k_B} \left(\frac{1}{T} - \frac{1}{T_{half}}\right)\right)} \quad (S8)$$

Where W is 3.37 eV and 2.75 eV during the heating and cooling processes, k_B is the Boltzmann constant, T is the temperature and T_{half} is 78.5 °C and 67.1 °C in the heating and cooling processes.

In camouflage or thermal management, VO₂ is usually directly heated by a thermal source, so the Maxwell-Garnett effect medium theory is more suitable for calculating the permittivity ϵ_{eff} during the phase change process, which is related to the metallization fraction f_{mVO_2} :

$$\epsilon_{eff} = \epsilon_s \frac{\epsilon_m (1 + 2f_{mVO_2}) - \epsilon_s (2f_{mVO_2} - 2)}{\epsilon_m (1 - f_{mVO_2}) + \epsilon_s (f_{mVO_2} + 2)} \quad (S9)$$

Where ϵ_m is the permittivity of metallic phase VO₂ and ϵ_s is the permittivity of semiconducting phase VO₂.

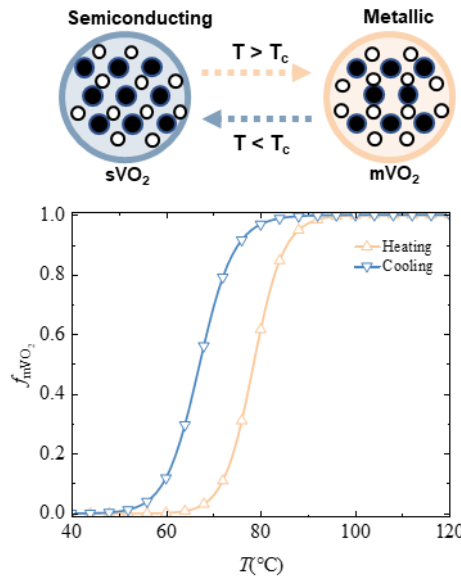


Fig. S3 The temperature-dependent metallization fraction f_{mVO_2} at the heating process and cooling down process.

As shown in Fig. S3, during heating, VO₂ starts to change from the amorphous to the crystalline phase when the temperature exceeds 60°C, becoming fully crystalline above 90°C. During cooling, VO₂ begins reverting to the amorphous phase below 80°C, with a complete phase change occurring below 50°C.

[1] Rensberg J, Zhang S, Zhou Y, et al. Active optical metasurfaces based on defect-engineered phase-transition materials. Nano letters, 2016, 16(2): 1050-1055

S5. The reliability of the numerical simulation results

The optimization and emissivity calculation of multilayer thin films are primarily performed using the transfer matrix method (TMM) [1, 2]. Additionally, the averaged emissivity results $\bar{\epsilon}_{3-5}$ and $\bar{\epsilon}_{8-14}$ of multilayers structure with IST gratings (shown in Fig. 2d of the manuscript) are calculated by an open-source rigorous coupled wave analysis method code based on Ref. [3].

To validate the reliability of our computational approach, the results are compared with those obtained from a well-established commercial electromagnetic field simulation software (Lumerical FDTD), as illustrated in Fig. S4. In the FDTD simulations, periodic boundary conditions (PBC) are applied along the x -direction, while perfect matching layer (PML) boundary conditions are used for the y -direction. A mesh size of 2 nm was employed in the simulations. The close agreement between the results from TMM, RCWA, and FDTD confirms the reliability of our computational methods.

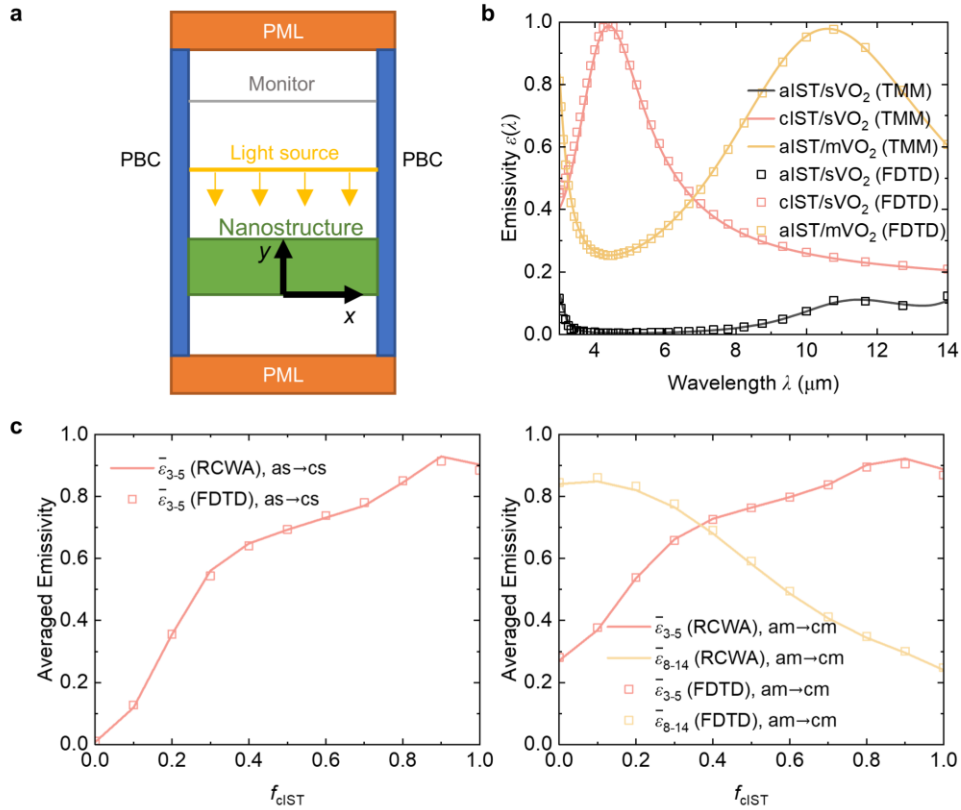


Fig. S4 The reliability of calculated results in the manuscript. **a.** The schematic of the model setup in the FDTD software. **b.** The spectral emissivity of the laminated structures under different phase transition states is verified, where the curves are calculated by TMM and the scatters are calculated by FDTD. **c.** The averaged emissivity of IST grating structure calculated by RCWA (lines) and FDTD (scatters).

- [1] S.J. Byrnes, Multilayer optical calculations, arXiv preprint arXiv, (2016) 1603.02720.
- [2] N.C. Passler, A. Paarmann, Generalized 4×4 matrix formalism for light propagation in anisotropic stratified media: study of surface phonon polaritons in polar dielectric heterostructures, Journal of the Optical Society of America B, 34 (2017) 2128-2139.
- [3] C. Kim, B. Lee, TORCWA: GPU-accelerated Fourier modal method and gradient-based optimization for metasurface design, Computer Physics Communications, 282 (2023) 108552.

S6. The net phase shift before and after IST and VO₂ phase change process

The phase shift before and after IST and VO₂ phase change process are shown in Fig. S5, and it proves that the modulation of emissivity is due to the F-P resonance.

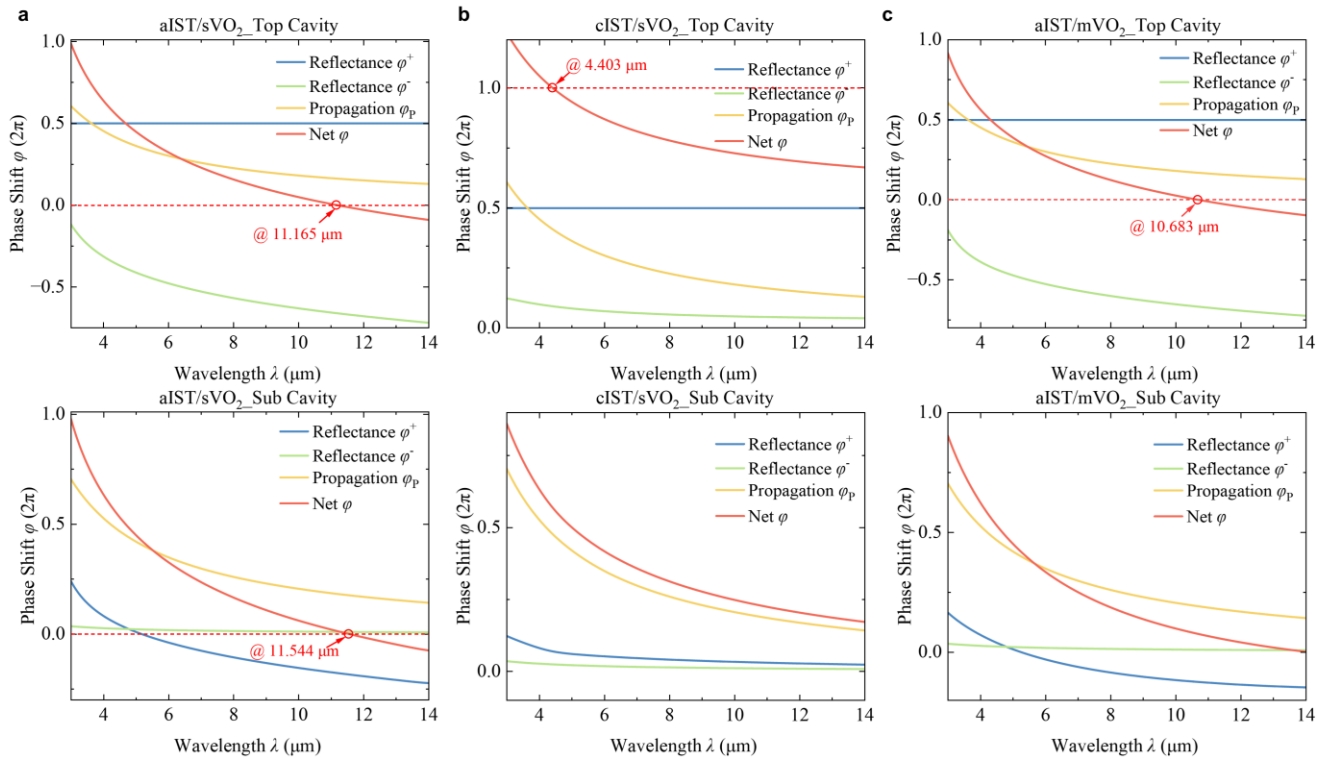


Fig. S5 The phase shift at the top and bottom cavity when the IST and VO₂ are at the a. aIST/sVO₂, b. cIST/sVO₂, and c. aIST/mVO₂ phase states.

S7. The structure parameters of the colored decoupled thermal emitter

Fig. S6 shows the detailed structure parameters, emissivity modulation and color characteristics of six examples in Fig. 5 in the manuscript. All examples maintain great infrared dual-band modulation (> 0.7) under different color characteristics. And the detailed IR spectral emissivity results are shown in Fig. S7.

	Top Layer	IST Layer	VO ₂ Layer	Middle Layer	$\Delta\bar{\epsilon}_{3-5}$	$\Delta\bar{\epsilon}_{8-14}$	CIE (x, y)	Color
E.g. 1	ZnS/Ge (43/216 nm)	(235 nm)	(178 nm)	ZnS (963 nm)	0.741	0.787	(0.475,0.323) [as]	
							(0.475,0.323) [am]	
							(0.476,0.322) [cs]	
E.g. 2	ZnS/Ge (31/218 nm)	(253 nm)	(176 nm)	Ge (463 nm)	0.752	0.797	(0.435,0.441) [as]	
							(0.435,0.441) [am]	
							(0.435,0.441) [cs]	
E.g. 3	ZnS/Ge (214/162 nm)	(250 nm)	(140 nm)	Ge (492 nm)	0.693	0.785	(0.310,0.495) [as]	
							(0.310,0.495) [am]	
							(0.311,0.494) [cs]	
E.g. 4	ZnS/Ge (59/216 nm)	(232 nm)	(147 nm)	Ge (487 nm)	0.744	0.776	(0.157,0.147) [as]	
							(0.157,0.147) [am]	
							(0.157,0.147) [cs]	
E.g. 5	ZnS/Ge (164/175 nm)	(289 nm)	(146 nm)	Ge (502 nm)	0.714	0.792	(0.282,0.160) [as]	
							(0.282,0.160) [am]	
							(0.282,0.159) [cs]	
E.g. 6	Ge/Ge (31/196 nm)	(249 nm)	(186 nm)	Ge (479 nm)	0.746	0.793	(0.317,0.340) [as]	
							(0.317,0.340) [am]	
							(0.318,0.340) [cs]	

Fig. S6 The detailed structure parameters and optical characteristics

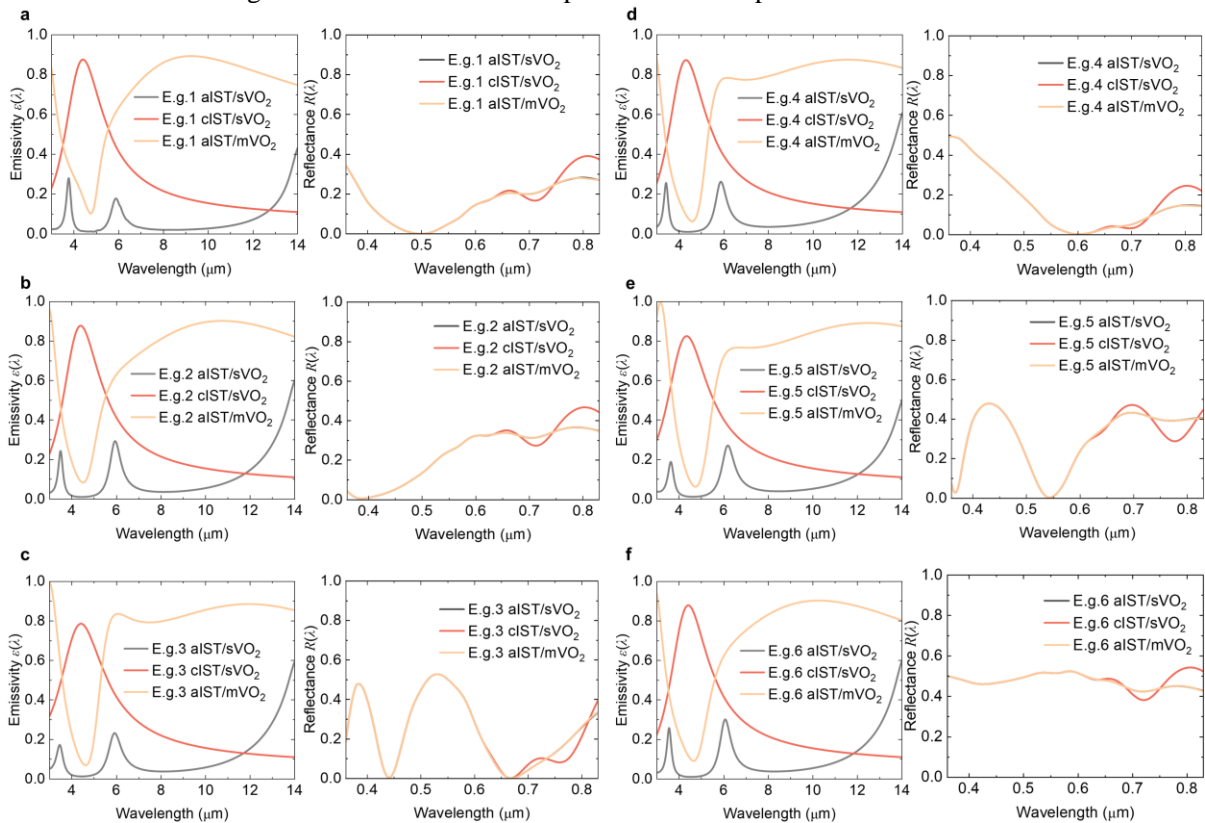


Fig. S7 The detailed IR spectral emissivity of six examples

The robustness of thickness of each layer is also discussed below. Fig. S8a and S8d show the actual and standard deviation results of spectral emissivity of emitter structure in Fig. 2a and E.g. 1 in Fig. 5a in the manuscript by increasing and decreasing the thickness of each layer by 5%. Fig. S8b and S8c more clearly show the results of infrared emissivity modulation in each infrared spectral. When the thickness of each layer increases and decreases by 5%, the infrared emissivity modulation ability changes no more than 1.87% in 3-5 μm and 3.2% in 8-14 μm . The color of E.g. 1 shows a slight shift but remains similar in Fig. S8e, demonstrating good stability that is unaffected by phase transitions in Fig. S8f.

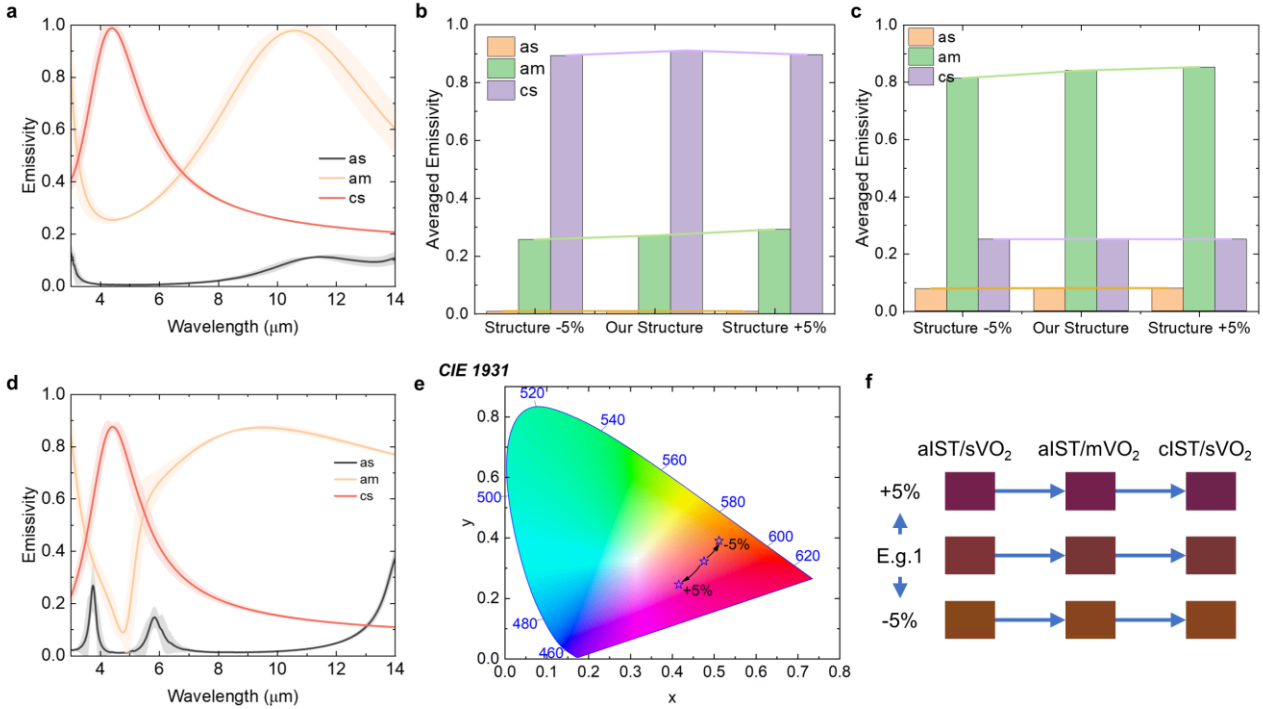


Fig. S8 **a**. The actual and standard deviation results of spectral emissivity of thermal emitter in Fig.3a in the manuscript by increasing and decreasing the thickness of each layer by 5%; **b**. Averaged emissivity of thermal emitter in Fig.3a in the manuscript in 3-5 μm by increasing and decreasing the thickness of each layer by 5%; **c**. Averaged emissivity of thermal emitter in Fig.3a in the manuscript in 8-14 μm by increasing and decreasing the thickness of each layer by 5%; **d**. The actual and standard deviation results of spectral emissivity of E.g. 1 thermal emitter in Fig.4b in the manuscript by increasing and decreasing the thickness of each layer by 5%. **e**. Color variation with thickness for each layer in E.g. 1. **f**. The detailed color results in different phase change states.

S8. The schematic of passive and active camouflage

To disguise the infrared image of the ‘NTU’ visible image as the one of a tank, we set different zones to different object temperatures T_{obj} and fill factor f_{cIST} . The schematic and parameters are shown in Fig. S9. To achieve independent temperature control for different camouflage units, an adaptive temperature control platform, as shown in Figure S9c, can be used. The temperature sensors detect the temperature of each unit and provide feedback to the computer, which then drives the thermoelectric components at the base to automatically adjust the applied voltage, thereby altering or stabilizing the temperature.

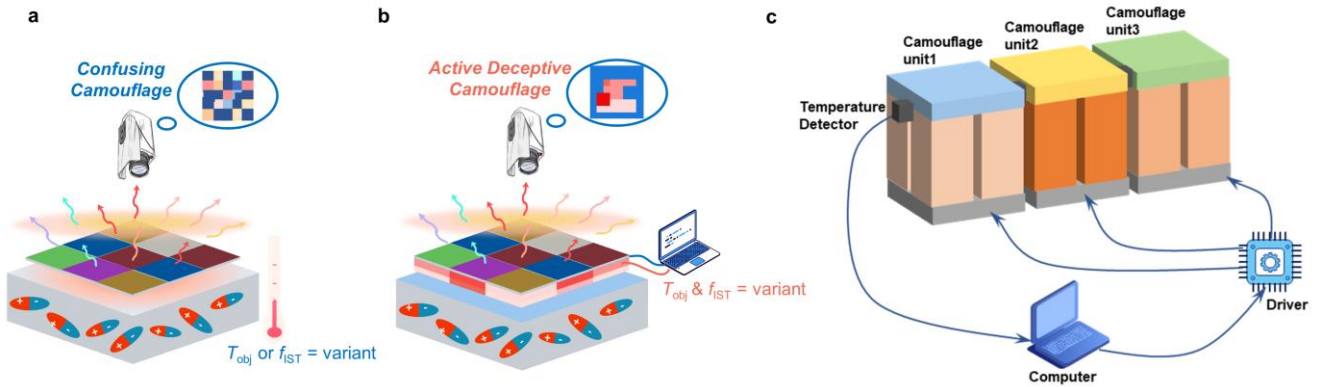


Fig. S9 **The schematic of passive confusing and active camouflage.** **a.** The schematic of passive confusing camouflage by modulating temperature or emissivity. **b.** The schematic of active deceptive camouflage by simultaneously modulating temperature and emissivity. **c.** The principle of the self-adaptive temperature modulation platform.

S9. Discussion on potential issues in the large-scale fabrication of tri-band decoupled thermal camouflage devices integrating IST and VO₂ phase change materials.

In this work, we use a design concept without lithography to greatly reduce the difficulty of large-scale device fabrication. Multilayer structure can be prepared on a large scale by magnetron sputtering or electron beam evaporation, which have been widely reported in Ref. [1-3]. It is important to note that the fabrication process for VO₂ requires high-temperature annealing [4], whereas IST is deposited using magnetron sputtering at room temperature [5]. By placing VO₂ as the bottom layer, we can first complete the VO₂ processing and high-temperature annealing. Once the temperature has cooled to room temperature, we can proceed with the IST fabrication. This design effectively accounts for the compatibility of VO₂ and IST in the manufacturing process. Besides, due to the metallic properties of cIST and local phase change characteristics of IST, it provides a feasible way to realize non-lithographic microstructure machining, avoiding complex lithography and other micro and nano machining methods. Recently, some works on non-volatile phase change materials IST have already demonstrated the feasibility of large-area phase change processing by IST [6, 7]. Thus the thermal camouflage device we proposed in this work has the potential to be scaled up for large-area fabrication for real-world applications.

Both VO₂ and IST have extremely short response time for switching between emissivity states. The response time of IST is about 50ns [5] and that of VO₂ can be femtosecond [8].

[1] J. Wang, Z. Wu, X. Sun, Z. Tang, C. Wang, F. Yu, Z. Zhao, J. Mao, Q. Zhang, F. Cao, Multi-band compatible camouflage enabled by phase transition modulation of flexible GST films, *Chemical Engineering Journal*, 499 (2024) 156128.

[2] M. Li, D. Liu, H. Cheng, L. Peng, M. Zu, Manipulating metals for adaptive thermal camouflage, *Science advances*, 6 (2020) eaba3494.

[3] X. Feng, M. Pu, F. Zhang, R. Pan, S. Wang, J. Gong, R. Zhang, Y. Guo, X. Li, X. Ma, Large-area low-cost multiscale-hierarchical metasurfaces for multispectral compatible camouflage of dual-band lasers, infrared and microwave, *Advanced Functional Materials*, 32 (2022) 2205547.

[4] X. Wang, Y. Cao, Y. Zhang, et al. Fabrication of VO₂-based multilayer structure with variable emittance, *Applied Surface Science*, 344 (2015) 230-235.

[5] A. Heßler.; S. Wahl.; T. Leuteritz, et al. In₃SbTe₂ as a programmable nanophotonics material platform for the infrared, *Nature Communications*, 12 (2021) 1-10.

[6] M. Giteau, L. Conrads, A. Mathwieser, R. Schmitt, M. Wuttig, T. Taubner, G.T. Papadakis, Switchable Narrowband Diffuse Thermal Emission With an In₃SbTe₂-Based Planar Structure, *Laser & Photonics Reviews*, (2024) 2401438.

[7] L. Conrads, N. Honné, A. Ulm, A. Heßler, R. Schmitt, M. Wuttig, T. Taubner, Reconfigurable and Polarization-Dependent Grating Absorber for Large-Area Emissivity Control Based on the Plasmonic Phase-Change Material In₃SbTe₂, *Advanced Optical Materials*, 11 (2023) 2202696.

[8] A. Cavalleri, T. Dekorsy, H.H.W. Chong, et al. Evidence for a structurally-driven insulator-to-metal transition in VO₂: A view from the ultrafast timescale, *Physical Review B—Condensed Matter and Materials Physics*, 70 (2004) 161102.